A Finite-Difference Transmission Line Matrix Method Incorporating a Nonlinear Device Model

ROBERT H. VOELKER, MEMBER, IEEE, AND
RONALD J. LOMAX, SENIOR MEMBER, IEEE

Abstract—**This paper describes a variable-mesh combination of the expanded-node transmission line matrix (TLM) and finite-difference time-domain (FD–TD) methods for solving time-domain electromagnetic problems. It retains the physical process of wave propagation and the numerical stability of the former, and has the computational efficiency of the latter. This full-wave finite-difference transmission line matrix (FD–TLM) method utilizes transmission lines of differing impedances to implement a three-dimensional variable mesh, which makes practical the simulation of structures having fine details, such as digital integrated circuits (IC's). Circuit models for lumped resistors, capacitors, diodes, and MESFET's have been developed and included for use in simulating digital and microwave IC's. The validity of the variable mesh implementation is verified by comparing an FD–TLM simulation of a picosecond pulse generator structure with electro-optical measurements, and the validity of the device model implementation is verified by comparing an FD–TLM simulation of a MESFET logic inverter with a SPICE simulation.**

I. INTRODUCTION

AS SEMICONDUCTORS and thus digital and microwave integrated circuits (IC's) become faster, the interconnections within the chips play an increasingly important part in circuit design. Picosecond-speed devices generate components in the tens to hundreds of gigahertz frequency range, where quasi-static electromagnetic analysis of interconnections is no longer accurate. What is needed is a full-wave, three-dimensional electromagnetic analysis. One such method is the transmission line matrix (TLM) method [1], which has been used for larger structures to determine properties such as resonant frequencies of cavities and microstrip dispersion. A related numerical method, the finite-difference time-domain (FD–TD) method [2], [3], has been used to simulate pulse propagation along conductors [4] and for electromagnetic scattering problems [5]. In most published descriptions of pulse propagation along microstrips, the conductors are wide enough that a uniform mesh can be used for the description of the structure. However, in digital IC's, the conductor widths are much smaller than the other dimensions of the structure, for example a 1-μm-wide conductor fabricated on a 500-μm-thick substrate. In this case a variable-mesh method is necessary to perform an accurate simulation without exceeding the memory and time limits of even supercomputers. A fine mesh is used around the conductors of interest and is smoothly graded into a coarse mesh near the integrated circuit package walls. Previous variable-mesh TLM methods [6], [7] have the disadvantage of requiring more computer resources when used to simulate IC's.

The ongoing refinement of the TLM method has taken place in parallel with the use of the FD–TD method for solving Maxwell's curl equations [8]. The finite-difference transmission line matrix (FD–TLM) method is a combination of both, offering a physical basis for wave propagation and the numerical stability of the TLM method and the computational efficiency of the FD–TD method.

Previous simulations of microstrips using the FD–TD method have been linear, where one end is excited with a field source and the fields are determined as they travel down the line to a linear termination [4]. By incorporating circuit models for lumped elements such as resistors, capacitors, diodes, and MESFET's in the FD–TLM method, more realistic simulations of high-speed, high-frequency IC's are achieved.

A short review of the conventional, three-dimensional expanded-node TLM method will be given, followed by a description of the three-dimensional variable-mesh TLM method that is based on transmission lines having differing impedances. This method will be transformed into the FD–TLM method by rewriting the TLM scattering matrices as finite differences, which will then be compared with the variable-mesh FD–TD method. A description of the circuit models for resistors, capacitors, diodes, and MESFET's follows. A variable-mesh FD–TLM simulation of a picosecond pulse generator structure will be compared to electro-optic measurements, and an FD–TLM simulation of a two-MESFET logic inverter will be compared with a SPICE simulation to demonstrate the validity of the variable mesh method and the MESFET model implementation.

Manuscript received June 20, 1988; revised October 25, 1989. This work was supported by the U.S. Army Research Office under the URI Program, Contract DAAL03-87-K-0007, and by the San Diego Supercomputer Center. As a Shell Doctoral Fellow, R. H. Voelker received support from the Shell Companies Foundation.

The authors are with the Center for High-Frequency Microelectronics, Department of Electrical Engineering and Computer Science, University of Michigan, Ann Arbor, MI 48109-2122.

IEEE Log Number 8933246.

0018-9480/90/0300-0302$01.00

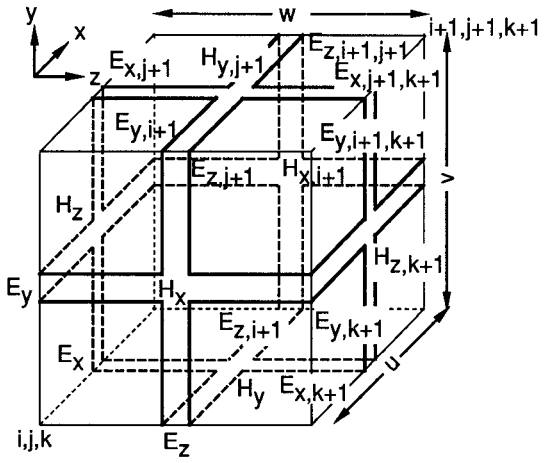

Fig. 1. Variable-mesh TLM cell. The six field components in the lower left corner are associated with i, j, k.

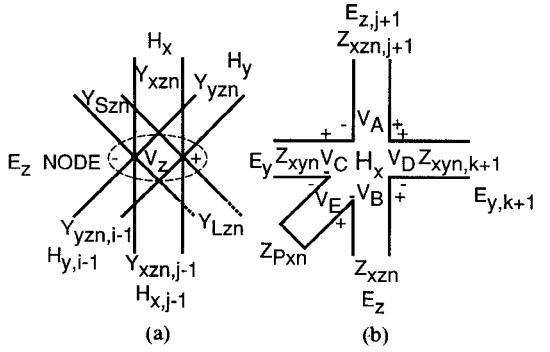

Fig. 2. (a) E_z shunt node. (b) H_x series node. The line with impedance Z_{xzn} is the same line in (a) having admittance Y_{xzn}. The permeability stub has impedance Z_{Pxn}.

II. Review of the Three-Dimensional Expanded-Node TLM Method

The conventional, three-dimensional expanded-node TLM method is based on pulses which travel along transmission lines interconnected as a three-dimensional matrix and then scatter at the intersections (nodes) into other connecting lines [1]. Fig. 1 shows a cell of six nodes that is repeated throughout the structure to be simulated. In the uniform-mesh case, $u = v = w = \Delta l$ and the lines all have length $\Delta l/2$ and the impedance of free space. There are two types of nodes: shunt nodes, where the voltage corresponds to an electric field; and series nodes, where the circulating current corresponds to a magnetic field. The computer program simulates wave propagation by performing scattering operations at all the shunt nodes at one time step and at all the series nodes half a time step later, yielding an explicit numerical method. In this manner, electromagnetic wave propagation is simulated, according to Huygens's principle [9]. Fig. 2 shows detailed drawings of the two nodes. The time step, τ, is the time it takes for a pulse to travel a length Δl along the lines.

The TLM method is based on an analogy between Maxwell's equations and the transmission line equations for the matrix [1]. Thus, by calculating the voltage at a shunt node and the current through a series node from the scattering matrices, the electric and magnetic fields are found, respectively.

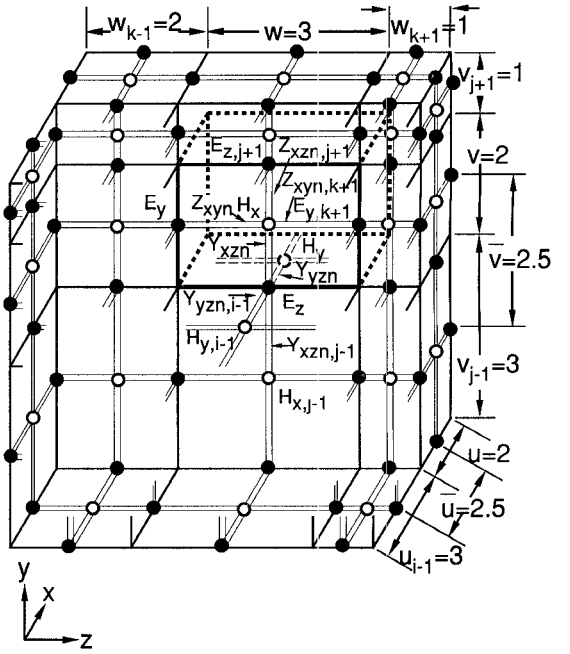

Fig. 3. An example of 18 variable-mesh TLM cells stacked together, emphasizing the interconnection of the H_x and E_z nodes with their neighbors: ○ magnetic node, ● electric node. The cell at i, j, k with dimensions $u = 2$, $v = 2$, $w = 3$ is highlighted. The stubs have been removed from the nodes for clarity.

Typically, a simulation of a structure is performed by applying a series of pulses to an electric field node and monitoring the voltages at other shunt nodes. A metal conductor is described by shorting out appropriate shunt nodes. Dielectric and losses, both isotropic and anisotropic, are described by adding shunt-connected open-circuited and loss stubs, respectively, to the shunt nodes [10]. Likewise, permeability variations are described by adding series-connected shorted stubs to the series nodes. The stubs are omitted from Fig. 1 for clarity. In [11]–[13], anisotropic permittivity and loss are represented instead by lumped capacitance and resistance at the electric field nodes, and permeability is represented by lumped capacitance at the magnetic field nodes.

III. The Variable-Mesh Three-Dimensional TLM Method

The variable-mesh TLM method uses the same interconnection of lines as the uniform-mesh TLM method. Cells represented by six nodes can have sides of different length and are stacked together to fill the entire space being simulated. Fig. 3 is an example of several variable-mesh cells filling a region of space. The lengths of the matrix cells are represented by u, v, and w. Each cell of discretized space is referenced by an i, j, k locator, but for clarity, only those positions which differ from i, j, or k are listed. Note that the cell dimension $u = u_{i,j,k}$ is independent of j and k; v is independent of i and k; and w is independent of i and j. Other symbols in Fig. 3 are defined later.

In [6], two techniques are described which implement a two-dimensional variable mesh in the TLM method, one called the stub loaded matrix, where the transmission lines are all of the same impedance, and the other called the hybrid matrix, where the matrix is composed of lines having different impedances. The three-dimensional stub loaded matrix method has the disadvantage that the simulation time step is made smaller than that in a uniform mesh having the same smallest grid spacing, by the ratio of the largest to the smallest grid spacing. This increases the number of iterations needed to perform a simulation for a given time period. However, by implementing the three-dimensional variable mesh using the hybrid matrix approach described below, the size of the time step is no longer dependent on the grading ratio, thus significantly reducing the computer time required to perform a simulation involving large grading ratios.

In the hybrid-matrix variable-mesh implementation, all transmission line segments connecting the nodes of the same type are of length Δl, set equal to the shortest length of the variable mesh, and stub loading is then added at the shunt nodes to represent the longer lines. Each transmission line segment, or link, has inductance per unit length of μ_0/h and capacitance per unit length of ϵ_0/h, where h is a velocity scaling factor to be determined later, and μ_0 and ϵ_0 are the permeability and permittivity, respectively, of free space. The propagation velocity of pulses on a link is thus proportional to h, and is equal to the speed of light in air when h is unity. Thus, the propagation delay along a link is

$$\tau = \frac{\Delta l}{v} = \frac{\Delta l}{h}\sqrt{\mu_0 \epsilon_0} \tag{1}$$

where v is the propagation velocity of pulses along a line. Equation (1) indicates that h is also a time scaling factor.

To simulate lines that are longer than Δl, the pulses must travel at a velocity proportional to the artificial line length to maintain pulse synchronization throughout the network. Thus

$$v = \frac{1}{\sqrt{L_0 C_0}} = \frac{l'}{\tau} \tag{2}$$

where v is the velocity of pulses on a line of artificial length l' having loaded inductance per unit length of L_0 and capacitance per unit length of C_0. From (1) and (2) it follows that

$$C_0 = \frac{(\Delta l)^2 \mu_0 \epsilon_0}{h^2 L_0 l'^2}. \tag{3}$$

Thus, the impedance $\sqrt{L_0/C_0}$ of this artificially extended line is proportional to the length l', which verifies that a variable mesh can be obtained from a network of transmission lines having different impedances. The computation of L_0 and C_0 is considered in the following.

A. Series Nodes

The relation between Maxwell's curl equations and the transmission line equations at a series node determines the inductance per unit length of the lines. As an example, consider the lines connecting the E_z shunt node to the H_x, $H_{x,j-1}$, H_y, and $H_{y,i-1}$ series nodes, which have inductances per unit length of $L_{xz0} = w\bar{\mu}_x/2\bar{u}$, $L_{xz0,j-1} = w\bar{\mu}_{x,j-1}/2\bar{u}$, $L_{yz0} = w\bar{\mu}_y/2\bar{v}$, and $L_{yz0,i-1} = w\bar{\mu}_{y,i-1}/2\bar{v}$, respectively, as derived in Appendix I, where $\bar{\mu}_x$, $\bar{u}$, and $\bar{v}$ are defined. The lines connecting series nodes to shunt nodes are identified using subscripts, with the first representing the type of series node and the second describing the shunt node. The 0 subscript indicates that the inductance is per unit length. In these expressions and elsewhere multiplication is assumed to have precedence over division.

Since $Z_n = Z/Z_0 = hl'L_0/\Delta l\mu_0$, then from (3) $C_0 = \epsilon_0 \Delta l/hl'Z_n$, where the subscript n means normalized to the impedance of free space, Z_0. Thus, the normalized line impedances are $Z_{xzn} = \bar{\mu}_x vwh/2\bar{u}\,\Delta l\mu_0$, $Z_{xzn,j-1} = \bar{\mu}_{x,j-1}v_{j-1}wh/2\bar{u}\,\Delta l\mu_0$, $Z_{yzn} = \bar{\mu}_y uwh/2\bar{v}\,\Delta l\mu_0$, and $Z_{yzn,i-1} = \bar{\mu}_{y,i-1}u_{i-1}wh/2\bar{v}\Delta l\mu_0$, and the line capacitances per unit length are $C_{xz0} = \epsilon_0 \Delta l/hvZ_{xyn}$, $C_{xz0,j-1} = \epsilon_0 \Delta l/hv_{j-1}Z_{xzn,j-1}$, $C_{yz0} = \epsilon_0 \Delta l/huZ_{yzn}$, and $C_{yz0,i-1} = \epsilon_0 \Delta l/hu_{i-1}Z_{yzn,i-1}$. Thus, the variable mesh requires using loaded lines having different impedances. The same concepts apply to the H_z node.

B. Shunt Nodes

Even though the transmission lines satisfy the inductance requirement at the series nodes, they do not necessarily have the correct capacitance to satisfy Maxwell's curl equations at the shunt nodes. At some shunt nodes, it is necessary to add capacitance in parallel with the four intersecting lines, which is performed by connecting an open-circuited $\Delta l/2$ long transmission line stub in shunt with the other lines.

Consider the E_z shunt node, which, from Appendix I, should have a total capacitance of

$$C_z = \frac{1}{4w}\left(\epsilon_z uw + \epsilon_{z,i-1}u_{i-1}v + \epsilon_{z,j-1}uv_{j-1} + \epsilon_{z,i-1,j-1}u_{i-1}v_{j-1}\right). \tag{4}$$

The stub must compensate for the deficiency in the intersecting lines' capacitance, and it has a capacitance of

$$C_{Sz} = C_z - \tfrac{1}{2}\left(C_{yz0}u + C_{yz0,i-1}u_{i-1} + C_{xz0}v + C_{xz0,j-1}v_{j-1}\right). \tag{5}$$

The lumped element approximation for an open-circuit stub of length $\Delta l/2$, at frequencies where the wavelength is relatively long compared to the stub, is a capacitance

$$C_{Sz} = \tfrac{1}{2}\tau Y_{Sz} \tag{6}$$

where Y_{Sz} is the stub admittance [6]. The admittance of a stub, normalized to the admittance of free space, $\sqrt{\epsilon_0/\mu_0}$, is

$$Y_{Szn} = \frac{2hC_{Sz}}{\epsilon_0 \Delta l} \tag{7}$$

from (1) and (6).

There is also an infinitely long loss stub attached to each E shunt node to represent the conductivity of the region in

space. For the E_z node, the loss stub has an admittance of

$$Y_{Lz} = G_z = \frac{1}{4w}\left(\sigma_z uv + \sigma_{z,i-1}u_{i-1}v + \sigma_{z,j-1}uv_{j-1} + \sigma_{z,i-1,j-1}u_{i-1}v_{j-1}\right) \quad (8)$$

from Appendix I. The same concepts also apply to the E_x and E_y shunt nodes.

Since the TLM method is based on the idea of simulating wave propagation by using networks of passive transmission lines, it is necessary that all stub admittances be nonnegative. This feature of the TLM method ensures numerical stability against exponentially increasing signals. To prevent the admittance of the stubs from being negative, h in the equations for transmission line capacitance is selected to be sufficiently large. However, h should be no larger than necessary, since the time step used in the simulation is $\tau = \Delta l/hc$, where c is the speed of light in free space, which means that more iterations would be needed in the simulation for an excessively large h.

That a constant value of h, independent of the grading ratio, will prevent the stubs from having negative admittance values, can be seen by considering (5) and substituting the equations for the capacitances, which gives

$$C_{Sz} = \bar{\epsilon}_z\frac{\bar{u}\bar{v}}{w} - \frac{(\Delta l)^2\mu_0\epsilon_0}{h^2 w}\cdot\left(\frac{\bar{v}}{u\bar{\mu}_y} + \frac{\bar{v}}{u_{i-1}\bar{\mu}_{y,i-1}} + \frac{\bar{u}}{v\bar{\mu}_x} + \frac{\bar{u}}{v_{j-1}\bar{\mu}_{x,j-1}}\right). \quad (9)$$

For media with permittivities and permeabilities equal to or greater than those of free space, (9) provides a stub with smallest capacitance (worst case) when these are equal to those of free space. Thus, using the free-space values in (9) and requiring C_{Sz} to be nonnegative, we obtain

$$h \geq \Delta l\sqrt{2\left(\frac{1}{uu_{i-1}} + \frac{1}{vv_{j-1}}\right)}. \quad (10)$$

Now, since the smallest dimension is Δl (i.e., $u \geq \Delta l$, $v \geq \Delta l$), $h = 2$ prevents the stub from having negative capacitance and thus negative admittance, for any grading ratio.

IV. Reformulation as a Finite-Difference Method

The uniform-mesh TLM method has been shown to be equivalent to the direct implementation of Maxwell's curl equations as finite differences by Johns [3]. Appendix II shows, in a perhaps more intuitive manner, how the variable-mesh TLM method can be rewritten as finite differences.

The scattering matrix for the variable-mesh TLM E_z shunt node is listed in Appendix II along with its reformulation into the finite-difference equation

$$V_z^{n+1} = \left(1 - \frac{2Y_{Lzn}}{K}\right)V_z^n + \frac{2Z_0}{K}\cdot\left(I_{x,j-1} - I_x + I_y - I_{y,i-1}\right)^{n+1/2} \quad (11)$$

where

$$K \equiv Y_{yzn} + Y_{yzn,i-1} + Y_{xzn} + Y_{xzn,j-1} + Y_{Szn} + Y_{Lzn} \quad (12)$$

and the Y are the admittances of the lines connected to this node, normalized to the admittance of free space and the superscripts represent the time step. Similarly, the scattering matrix for the variable-mesh TLM H_x series node is listed in Appendix II, which yields the finite-difference equation

$$I_x^{n+1/2} = I_x^{n-1/2} + \frac{2}{Z_0 M}\left(V_z - V_{z,j+1} + V_{y,k+1} - V_y\right)^n \quad (13)$$

where

$$M \equiv Z_{xzn,j+1} + Z_{xzn} + Z_{xyn} + Z_{xyn,k+1} + Z_{Pxn} \quad (14)$$

and the Z are the impedances of the lines connected to this node, normalized to the impedance of free space. Thus, the variable-mesh TLM method has been converted into the variable-mesh FD–TLM method.

The three-dimensional variable-mesh FD–TLM method requires much less in the way of computer resources than the three-dimensional extension of the variable-mesh TLM method proposed by Al-Mukhtar and Sitch [6]. The present method uses only 18 memory locations per six-field cell versus 26 (or 30 if anisotropic permittivity and permeability are considered) in [6]. Moreover, the present method requires only 36 floating point operations per cell versus 69 in [6]. Even more significant is that the time step in the present method is independent of the mesh grading ratio, unlike [6], where the time step size is reduced in proportion to the ratio of the largest to smallest mesh spacing, thereby requiring many more iterations for the same total simulation period. For example, in the DCFL inverter simulation described later, there is a mesh cell with dimensions $u = w = 1$ μm and $v = 256$ μm, with $\epsilon_r = 1$, yielding a time step of 1.67×10^{-15} s for the present method, and by (7) and (24(b)) in [6], 6.51×10^{-18} s for the latter method. Thus, the variable-mesh FD–TLM method is much more computationally efficient for IC simulation than the method described in [6].

The variable-mesh FD-TLM method also has advantages over the three-dimensional variable-mesh punctual node method [7] for IC simulation. The punctual node method has a very complex 15×15 scattering matrix at each six-field node. Although for regular cavities containing only one or two dielectrics these are easily simplified, they are very unwieldy to store in memory and multiply by the node voltages for structures having elaborate conductor and dielectric boundary conditions found in IC's. Thus, less computer memory and time would be required for an IC simulation using the variable-mesh FD–TLM method. This, as all other discrete mesh methods, introduces numerical dispersion, which is a function of the mesh size variation. Although there is reasonable agreement between the FD–TLM method and other approaches, as discussed later, further study of this effect is needed.

V. Direct Implementation of Maxwell's Equations as Finite Differences and Comparison with the Variable-Mesh FD–TLM Method

Maxwell's curl equation for the E_z field is

$$\frac{\partial H_y}{\partial x} - \frac{\partial H_x}{\partial y} = \bar{\epsilon}_z \frac{\partial E_z}{\partial t} + \bar{\sigma}_z E_z \tag{15}$$

which, when truncated Taylor series are used for the partial derivatives as follows,

$$\frac{\partial H_y}{\partial x} \approx \frac{1}{\bar{u}} \left(H_y - H_{y,i-1} \right)^{n+1/2} \tag{16}$$

$$\frac{\partial H_x}{\partial y} \approx \frac{1}{\bar{v}} \left(H_x - H_{x,j-1} \right)^{n+1/2} \tag{17}$$

$$\frac{\partial E_z}{\partial t} \approx \frac{1}{\Delta T} \left(E_z^{n+1} - E_z^n \right) \tag{18}$$

and the time average is used for E_z in the term containing the conductivity,

$$E_z \approx \tfrac{1}{2} \left(E_z^{n+1} + E_z^n \right) \tag{19}$$

gives

$$E_z^{n+1} = \left(1 - \frac{2\bar{\sigma}_z}{(2\bar{\epsilon}_z/\Delta T) + \bar{\sigma}_z} \right) E_z^n + \left(\frac{2}{(2\bar{\epsilon}_z/\Delta T) + \bar{\sigma}_z} \right) \cdot \left(\frac{H_y - H_{y,i-1}}{\bar{u}} + \frac{H_{x,j-1} - H_x}{\bar{v}} \right)^{n+1/2}. \tag{20}$$

In isotropic loss-free regions, this is similar to the approach used in [5], but (19) is treated differently, as is also the averaging of conductivity, permittivity, and permeability. When similar approximations are used, the equation

$$\frac{\partial E_z}{\partial y} - \frac{\partial E_y}{\partial z} = -\bar{\mu}_x \frac{\partial H_x}{\partial t} \tag{21}$$

gives

$$H_x^{n+1/2} = H_x^{n-1/2} + \frac{\Delta T}{\bar{\mu}_x} \left(\frac{E_{y,k+1} - E_y}{w} + \frac{E_z - E_{z,j+1}}{v} \right)^n. \tag{22}$$

The electromagnetic fields at the E_z shunt node and the surrounding H_x and H_y series nodes in the FD–TLM method are related to the analogous node voltage and currents by

$$V_z = E_z w, \quad I_x = H_x \bar{u}, \quad I_y = H_y \bar{v}. \tag{23}$$

Substitution of these and the equations for the admittances of the lines into the variable-mesh FD–TLM method (11) yields (20) when ΔT in the FD–TD method is equated to $\Delta l \sqrt{\mu_0 \epsilon_0}/h$ in the FD–TLM method. The methods are thus seen to be identical. For example, if h is selected as 2.0 in the FD–TLM method for a simulation involving free space as the medium, then the corresponding FD–TD time step would be $\Delta T = \Delta l/2c$. According to [2], for the three-dimensional uniform-mesh FD–TD method, the time step must meet the criterion $\Delta T \leq \Delta l/\sqrt{3}\,c$ for stability. Thus, the FD–TLM method has an inherent extra margin of stability.

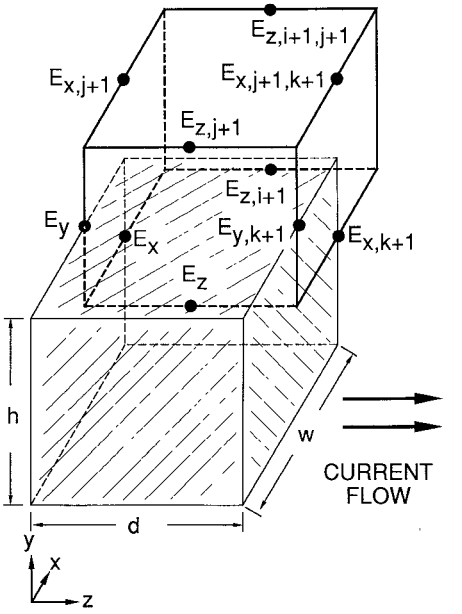

Fig. 4. Implementation of lumped resistance at an E_z node.

For the H_x series node and the surrounding E_y and E_z shunt nodes in the FD–TLM method, the electromagnetic fields are related to the node voltages and current by

$$V_z = E_z w \qquad V_y = E_y v \qquad I_x = H_x \bar{u} \tag{24}$$

where $\bar{u}$ is the averaged length of the cell surrounding the H_x node. Substitution of these into the variable-mesh FD–TLM method, (13), gives (22) after the equations for the impedances of the lines connecting at the H_x node are substituted and the same value of ΔT is used. The numerical stability considerations are thus the same as those for the E_z node.

VI. Incorporation of Resistors and Capacitors in the FD–TLM Method

Basically, a resistance can be thought of as a region of conducting media with electrodes at either end. If the region is rectangular, sandwiched between highly conductive end plates, and small compared to the wavelength, then it can be considered a lumped resistor with value $R = d/\sigma h w$, where d, h, and w are the dimensions of the rectangular region and σ is the conductivity. In the FD–TLM method, an example of the implementation of a lumped resistor with conductivity in the z direction is shown in Fig. 4. Given the resistance desired and the dimensions of the region, then the value calculated for σ_z is used to determine the admittance for the FD–TLM loss stub at the E_z node. The shaded volume is the region of influence of the E_z node, which extends half the distance in the x and y directions to the neighboring E_z nodes. If just one E_z node has conductance, then the lumped conductance is an infinitely thin filament, due to the discretized nature of the FD–TLM mesh. However, if several neighboring E_z nodes in the same $x-y$ plane have conductance, then a lumped two-dimensional sheet resistor or three-dimensional block resistor is formed.

This concept can be extended to lumped capacitors in the FD–TLM method. Considering conductive plates at the left and right ends of the region surrounding the E_z node in Fig. 4, the parallel-plate capacitance is $C = \epsilon_0 \epsilon_{rz} hw/d$. From the desired value of C and the dimensions of the region, ϵ_{rz} is determined, which then specifies the admittance of the permittivity stub in the FD–TLM method.

VII. Incorporation of the Ideal Diode Model in the FD–TLM Method

The ideal diode equation is $I = I_S(e^{V/\eta V_{th}} - 1)$, where I and I_S are the diode terminal and saturation currents, respectively, V and V_{th} are the diode terminal and thermal voltages, respectively, and η is the diode ideality factor. This diode is implemented in the FD–TLM method at an E_z node, for example, by monitoring the electric field at the node and multiplying by the distance d to find the diode voltage. This voltage is then substituted in the ideal diode equation to find the current that should flow through the diode. From the diode voltage and current, the conductance to be implemented at the node is then determined. In this explicit method, there is a time lag of ΔT between the calculation of the diode voltage and the adjustment of the diode conductance. However, this lag is so small, e.g., 1.7 fs for a 1 μm FD–TLM mesh spacing, compared to the events of interest, such as the 10 ps switching speed of transistors, that the diode's behavior appears essentially continuous in time. Other functional relationships between I and V can be incorporated similarly.

The capacitance of a diode varies with voltage and thus can be incorporated by adjusting the dielectric constant at the E_z node, for example, to give the capacitance required by the equation relating diode capacitance to voltage.

Although the implementation of lumped resistors, capacitors, diodes, and transistors in the TLM method has been proposed previously [14], the emphasis in this reference was on solving a network problem in which the goal was to find novel lumped circuit solution techniques as an alternative to more conventional circuit simulators, rather than solving a three-dimensional electromagnetics problem.

VIII. Incorporation of a GaAs MESFET Model in the FD–TLM Method

The GaAs MESFET model used in the UM-SPICE (University of Minnesota SPICE) (Fig. 5(a)) [15] circuit simulator program has been incorporated into the FD–TLM method by using the concepts of voltage-variable lumped resistance and capacitance. The drain current in this model is related to gate and drain voltages by

$$I_{DS} = \beta_0 (V_{GS} - V_T)^2 (1 + \lambda V_{DS}) \tanh\left[\frac{G_{CHI} V_{DS}}{\beta_0 (V_{GS} - V_T)^2}\right] \tag{25}$$

where the coefficients are defined in [15].

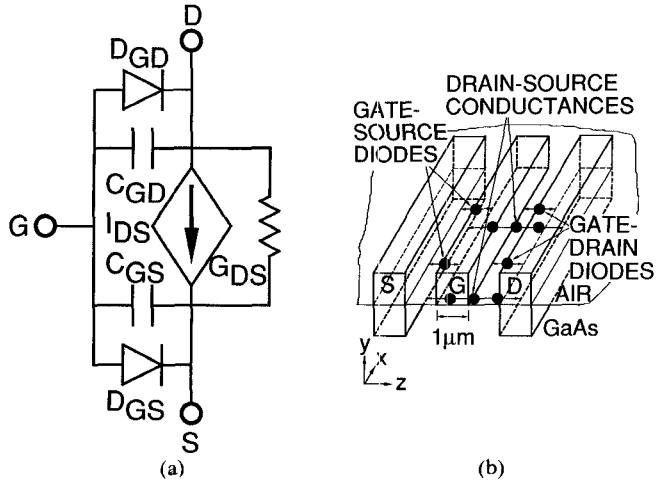

Fig. 5. (a) Circuit model for GaAs MESFET implemented in the FD–TLM method. (b) GaAs MESFET circuit model incorporated in the FD–TLM method at two locations along the width of a 10×1 μm gate MESFET. The E_z nodes are shown as ● for reference.

Fig. 5(b) shows the implementation of the MESFET model in the FD–TLM mesh. In applications considered so far, metal source and drain electrodes are typically 1 μm wide and extend 1 μm above and below the substrate, while the gate electrode extends 1 μm above the substrate. The spacing of the electrodes is typically 1 μm. The gate–source and gate–drain voltages are calculated from the fields between these electrodes, and the drain–source voltage is in turn calculated from these voltages. The gate–source and gate–drain diodes are implemented as described before and the drain–source current is implemented by calculating the required drain current from (25) and then subsequently adjusting the drain–source conductance to be equal to I_{DS}/V_{DS}.

Two and three of these lumped models have been used along the width of 10 and 20 μm wide MESFET's, respectively, with good results. To accurately model the effect of phase shift along the electrodes of wide (e.g., 0.5 mm) MESFET's in MMIC's, perhaps 20 or more of these lumped models could be distributed along the width. Several simulations of complete IC's having as many as ten MESFET's based on this MESFET model have been shown to be accurate and free from any kind of numerical instabilities [16], [17].

IX. Simulation of a Picosecond Pulse Generator Structure

To verify the results of the variable-mesh FD–TLM method, a simulation of a picosecond pulse generator constructed from a coplanar waveguide containing a shunt discontinuity is compared to electro-optical measurements [18]. Fig. 6 shows the layout of the pulse generator simulated. The actual pulse generator works on the principle of applying a dc voltage to charge the center conductor of the coplanar waveguide to the left of the photoconductive gap and then exciting the gap with a 120 fs duration laser pulse. The photoconductivity of the GaAs causes the line to discharge and a short-rise-time, long-decay-time step

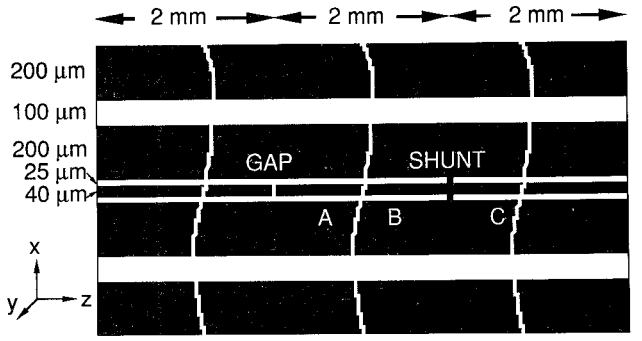

Fig. 6. Compressed layout of the picosecond pulse generator.

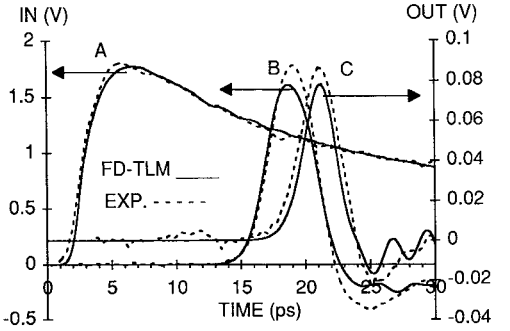

Fig. 7. FD–TLM simulated and measured input and output pulses of the picosecond pulse generator.

TABLE I
VARIABLE-MESH DISCRETIZATION OF THE PICOSECOND PULSE GENERATOR

x-axis		y-axis		z-axis	
cell No.	μm	cell No.	μm	cell No.	μm
1	122	1	212	1–19	80
2	52	2	96	20–24	40
3–4	26	3–4	48	25–30	20
5	48	5–6	24	31–36	10
6	26	7–9	12	37–78	5
7	56	10–13	6	79–88	10
8	48	14	12	89–167	20
9–10	24	15	24	168–177	10
11–12	12	16	48	178–219	5
13–16	6	17	96	220–229	10
17–21	5	18–19	192	230–319	20
22–25	5.7	20–21	384		

pulse travels rightward toward the shunt. When the step pulse reaches the shunt, only the high-frequency components are transmitted. Thus, the shunt converts a long-decay-time input pulse into a short-decay-time output pulse.

The open structure on which measurements were performed consists of a 0.35 μm gold layer on top of 0.05 μm of titanium on a 0.5-mm-thick GaAs substrate. Seven coplanar waveguide structures were side by side on the chip separated by 100 μm. One of these was approximated in the FD–TLM simulation as shown in Fig. 6 with infinitely thin conductors having loss equivalent to 0.35 μm gold. To better represent the actual structure, the ground planes of the neighboring coplanar waveguides were also included in the simulation.

The structure was simulated in a perfectly conducting metal rectangular package having dimensions $1.09\times1.844\times6.0$ mm^3 (x, y, z) and discretized with $25\times21\times319$ (x, y, z) cells as described in Table I. A magnetic wall was used down the center of the coplanar waveguide to halve the number of calculations. The 10-μm-long photoconductive gap and the 20-μm-wide shunt are located 2.0 and 4.0 mm from the left end of the structure.

The simulation was performed by applying a z-directed electric field in the gap in the plane of the coplanar waveguide to generate a voltage

$$V(t) = 0.4t\left[\exp(-0.17t)+1.8\exp(-0.38t)+0.24\exp(-0.044t)\right] \quad (26)$$

where t is the time in picoseconds, as an approximation to the voltage step generated by the photoconductor excitation.

Fig. 7 shows the FD–TLM simulation and electro-optical measurements of the voltages along the coplanar waveguide at points A, B, and C, which are at 205 μm past the gap, 200 μm before the shunt, and 190 μm past the shunt, respectively. In the simulation, the voltage along the coplanar waveguide was calculated by integrating the x-directed electric field from the center conductor to the coplanar ground plane. In the measurement, the voltage was determined by the same x-directed electric field sampled with an electro-optic probe placed across the center conductor and ground plane. The accuracy of the electro-optic probe placement was ±0.03 mm, corresponding to an accuracy in time of about ±0.27 ps. The amplitude measurement accuracy was roughly ±20 percent. Thus, there is good agreement between the variable-mesh FD–TLM simulation and electro-optical measurements.

X. SIMULATION OF A DCFL INVERTER

To get independent verification of the accuracy of the incorporation of an MESFET circuit model in the variable-mesh FD–TLM method, FD–TLM and UM-SPICE simulations were performed on the direct-coupled FET logic (DCFL) inverter shown in Fig. 8. The dashed lines represent the variable mesh, which has a 2:1 grading ratio at adjacent cells and a smallest size of 1 μm. The chip was simulated on a 0.513-mm-thick GaAs substrate mounted at the bottom of a $1.05\times1.538\times1.045$ mm^3 (x, y, z) perfectly conducting rectangular cavity discretized with $55\times25\times43$ (x, y, z) cells as described in Table II.

The conductors in Fig. 8 are all 1 μm thick and perfectly conducting, although they could have been made lossy in the FD–TLM method. The crosshatched areas are 1-μm-thick resistors. The source resistor, for example, is modeled

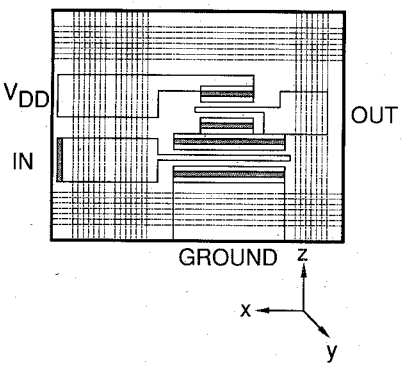

Fig. 8. Variable-mesh layout of the DCFL inverter.

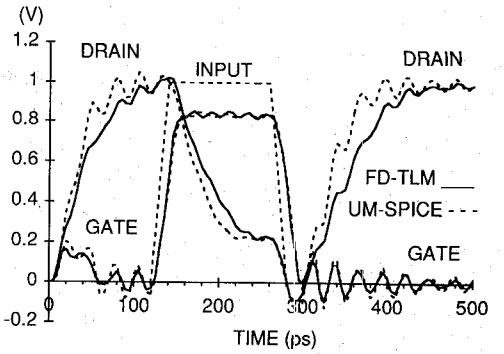

Fig. 9. FD–TLM and UM-SPICE simulation results for the DCFL inverter.

TABLE II
VARIABLE-MESH DISCRETIZATION OF THE DCFL INVERTER

x-axis		y-axis		z-axis	
cell No.	μm	cell No.	μm	cell No.	μm
1–3	128	1–3	128	1–3	128
4	64	4	64	4	64
5	32	5	32	5	32
6	16	6	16	6	16
7	8	7	8	7	8
8	4	8	4	8	4
9	2	9	2	9	2
10–37	1	10–15	1	10–34	1
38	2	16	2	35	2
39	4	17	4	36	4
40	8	18	8	37	8
41	16	19	16	38	16
42	32	20	32	39	32
43	64	21	64	40	64
44–45	128	22	128	41–43	128
46	64	23–25	256		
47	32				
48	16				
49	8				
50	4				
51	2				
52–55	1				

as a three-dimensional block of resistive material having dimensions $1\mu m \times 1\mu m \times 8\mu m$ (x, y, z) and is described with $1 \times 2 \times 9$ (x, y, z) nodes. The 20×1 μm enhancement mode driver MESFET has threshold voltage $V_T = 0.21$ V, transconductance parameter $\beta_0 = 0.00287$ A/V^2, parasitic source and drain resistances $R_S = R_D = 50\ \Omega$, and zero-bias gate–source and gate–drain capacitances $C_{GS0} = C_{GD0} = 9.59$ fF. The 10×1 μm depletion mode load MESFET has $V_T = -0.61$ V, $\beta_0 = 0.00103$ A/V^2, $R_S = R_D = 100\ \Omega$, and $C_{GS0} = C_{GD0} = 7.77$ fF.

The FD–TLM simulation was performed by applying an electric field in the x direction between the cavity wall and the conductor marked V_{DD} so that a 1 V step with a 40 ps rise time was generated. Likewise, the input signal source was represented by applying an electric field in the x direction between the cavity wall and the 100 Ω source resistor.

Fig. 9 shows good agreement between the variable-mesh FD–TLM and UM-SPICE simulations for the voltages calculated at the gate and drain of the driver transistor. When the V_{DD} line was raised to 1 V, the driver drain voltage went to 1 V in response, since the input voltage was 0 V. At 120 ps, the input voltage switched to 1 V and the driver drain voltage started falling toward 0 V. At 260 ps, the input voltage switched to 0 V, causing the driver drain voltage to progress toward 1 V. The voltages in the FD–TLM method were calculated by integrating the vertical electric field along the path from the ground plane to the MESFET electrodes. The parasitic capacitances and inductances used in the UM-SPICE simulation were estimated using formulas of Van Tuyl [19] and formulas in [20].

XI. CONCLUSIONS

Two new contributions to the TLM electromagnetic field solution method have been discussed. First, a new variable-mesh full-wave combination of the transmission line matrix and finite-difference time-domain numerical methods, called the finite-difference transmission line matrix (FD–TLM) method, has been developed and its relationship to its parent methods has been discussed. It has the computational efficiency of the FD–TD method, but retains characteristics of the TLM method: intuitive formalism of wave propagation based on Huygen's principle, and numerical stability. Second, semiconductor diodes and GaAs MESFET's as well as resistors and capacitors have been incorporated into the variable-mesh FD–TLM method, allowing a unified, three-dimensional full-wave electromagnetic simulation of microwave and high-speed digital integrated circuits.

Comparison of simulation and experimental electro-optical measurements of a picosecond pulse generator shows good agreement, as do FD–TLM and UM-SPICE simulations of a DCFL inverter integrated circuit. Although for this IC the UM-SPICE simulation based on a quasi-static calculation of capacitance and inductance is sufficient, because of the relatively small overall dimensions involved, a full-wave method would be needed if the circuit had larger dimensions.

The variable-mesh FD–TLM method incorporating semiconductor devices is easier to use for IC simulation compared to other electromagnetic methods, since it is general purpose and does not require analytical approximations limiting it to certain special cases of conductor geometries. A computer program has been written and used in the layout of the conductor geometries on a computer-aided-design workstation display screen to generate the data set necessary for variable-mesh FD–TLM simulations of IC's.

Appendix I
Analogy Between Maxwell's Curl Equations and the Circuit Equations

A. Series Nodes

Applying Kirchhoff's voltage law to the H_x node equivalent circuit shown in Fig. 10 gives

$$\frac{1}{w}\frac{\partial V_z}{\partial y} - \frac{1}{v}\frac{\partial V_y}{\partial z} = -\frac{L_{px}}{vw}\frac{\partial I_x}{\partial t} \tag{A1}$$

where $L_{px} = L_{xy} + L_{xz}$. Comparing this to Maxwell's curl equation,

$$\frac{\partial E_z}{\partial y} - \frac{\partial E_y}{\partial z} = -\bar{\mu}_x \frac{\partial H_x}{\partial t} \tag{A2}$$

and letting $E_z = V_z/w$, $E_y = V_y/v$, and $H_x = I_x/\bar{u}$, where $\bar{u} = (u + u_{i-1})/2$, gives $L_{px} = \bar{\mu}_x vw/\bar{u}$, where

$$\bar{\mu}_x = \frac{2\bar{u}\mu_{x,i-1}\mu_x}{u_{i-1}\mu_x + u\mu_{x,i-1}} \tag{A3}$$

and μ_x, μ_y, μ_z are the permeabilities at the series nodes

Assume that L_{xy} and L_{xz} are both proportional to $vw/\bar{u}$. Thus, $L_{xy} = L_{xz} = L_{px}/2$, $L_{xy0} = \bar{\mu}_x v/2\bar{u}$, and $L_{xz0} = \bar{\mu}_x w/2\bar{u}$. The other H nodes are handled similarly.

B. Shunt Nodes

For the equivalent circuit of the E_z shunt node shown in Fig. 11, Kirchhoff's current law gives

$$\frac{1}{\bar{v}}\frac{\partial I_y}{\partial x} - \frac{1}{\bar{u}}\frac{\partial I_x}{\partial y} = \frac{G_z}{\bar{u}\bar{v}}V_z + \frac{C_z}{\bar{u}\bar{v}}\frac{\partial V_z}{\partial t}. \tag{A4}$$

Comparing this to Maxwell's curl equation,

$$\frac{\partial H_y}{\partial x} - \frac{\partial H_x}{\partial y} = \bar{\sigma}_z E_z + \bar{\epsilon}_z \frac{\partial E_z}{\partial t} \tag{A5}$$

and letting $H_x = I_x/\bar{u}$, $H_y = I_y/\bar{v}$, and $E_z = V_z/w$, where $\bar{u} = (u + u_{i-1})/2$ and $\bar{v} = (v + v_{j-1})/2$, gives $G_z = \bar{\sigma}_z \bar{u}\bar{v}/w$

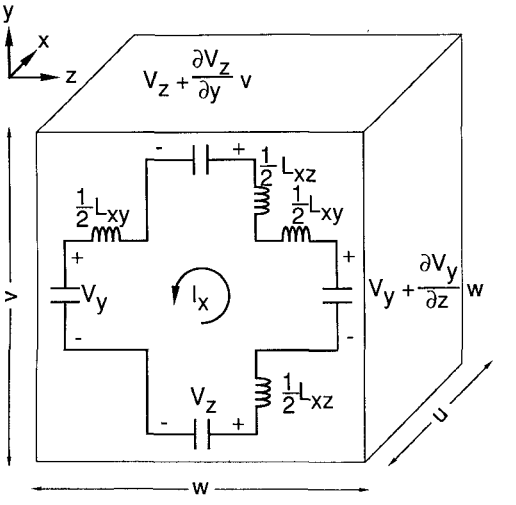

Fig. 10. Equivalent circuit for the H_x series node.

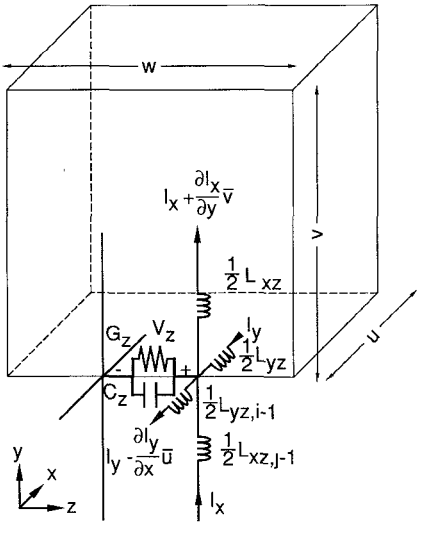

Fig. 11. Equivalent circuit for the E_z shunt node.

and $C_z = \bar{\epsilon}_z \bar{u}\bar{v}/w$. The weighted averages for the permittivity and conductivity are given as

$$\bar{\epsilon}_z = \frac{\epsilon_z uv + \epsilon_{z,i-1}u_{i-1}v + \epsilon_{z,j-1}uv_{j-1} + \epsilon_{z,i-1,j-1}u_{i-1}v_{j-1}}{uv + u_{i-1}v + uv_{j-1} + u_{i-1}v_{j-1}} \tag{A6}$$

and

$$\bar{\sigma}_z = \frac{\sigma_z uv + \sigma_{z,i-1}u_{i-1}v + \sigma_{z,j-1}uv_{j-1} + \sigma_{z,i-1,j-1}u_{i-1}v_{j-1}}{uv + u_{i-1}v + uv_{j-1} + u_{i-1}v_{j-1}}. \tag{A7}$$

The other E nodes are handled similarly.

Appendix II
Derivation of the Finite-Difference Form of the TLM Method for the Nodes

The voltage V_z^{n+1} must be found in terms of the voltage V_z^n and the currents at time $t = (n + \frac{1}{2})\Delta T$ at the four neighboring series nodes. The superscripts indicate the time. The relation between the pulses incident to and

reflected from the shunt node (see Fig. 2(a)) is given by

$$\begin{bmatrix} V_1 \\ V_2 \\ V_3 \\ V_4 \\ V_5 \end{bmatrix}^r = [S]_{\mathrm{Sh}} \begin{bmatrix} V_1 \\ V_2 \\ V_3 \\ V_4 \\ V_5 \end{bmatrix}^i \tag{A8}$$

where

$$[S]_{\mathrm{Sh}} = \frac{2}{K} \begin{bmatrix} Y_{yzn} & Y_{yzn,i-1} & Y_{xzn} & Y_{xzn,j-1} & Y_{Szn} \\ Y_{yzn} & Y_{yzn,i-1} & Y_{xzn} & Y_{xzn,j-1} & Y_{Szn} \\ Y_{yzn} & Y_{yzn,i-1} & Y_{xzn} & Y_{xzn,j-1} & Y_{Szn} \\ Y_{yzn} & Y_{yzn,i-1} & Y_{xzn} & Y_{xzn,j-1} & Y_{Szn} \\ Y_{yzn} & Y_{yzn,i-1} & Y_{xzn} & Y_{xzn,j-1} & Y_{Szn} \end{bmatrix} - [I] \tag{A9}$$

and

$$K \equiv Y_{yzn} + Y_{yzn,i-1} + Y_{xzn} + Y_{xzn,j-1} + Y_{Szn} + Y_{Lzn}. \tag{A10}$$

Voltages V_1, V_2, V_3, V_4, and V_5 are defined with the same polarity as V_z at the E_z node along the lines having admittances Y_{yzn}, $Y_{yzn,i-1}$, Y_{xzn}, $Y_{xzn,j-1}$, and Y_{Szn}, respectively. The voltage across the shunt node at time $t = (n+1)\Delta T$ is written as

$$V_z^{n+1} = \frac{2}{K}\left(Y_{yzn}V_{1i} + Y_{yzn,i-1}V_{2i} + Y_{xzn}V_{3i} + Y_{xzn,j-1}V_{4i} + Y_{Szn}V_{5i}\right)^{n+1}. \tag{A11}$$

The currents at the neighboring series nodes are related to the voltages at the shunt node by

$$I_{x,j-1}^{n+1/2} = -\frac{Y_{xzn,j-1}}{Z_0}\left(V_{4r}^n - V_{4i}^{n+1}\right) \tag{A12}$$

$$I_{y,i-1}^{n+1/2} = \frac{Y_{yzn,i-1}}{Z_0}\left(V_{2r}^n - V_{2i}^{n+1}\right) \tag{A13}$$

$$I_x^{n+1/2} = \frac{Y_{xzn}}{Z_0}\left(V_{3r}^n - V_{3i}^{n+1}\right) \tag{A14}$$

$$I_y^{n+1/2} = -\frac{Y_{yzn}}{Z_0}\left(V_{1r}^n - V_{1i}^{n+1}\right). \tag{A15}$$

Substituting (A12)–(A15) into (A11) gives

$$V_z^{n+1} = \frac{2Z_0}{K}\left(I_{x,j-1} - I_x + I_y - I_{y,i-1}\right)^{n+1/2} + \frac{2}{K}\left(Y_{yzn}V_{1r} + Y_{yzn,i-1}V_{2r} + Y_{xzn}V_{3r} + Y_{xzn,j-1}V_{4r} + Y_{Szn}V_{5r}\right)^n. \tag{A16}$$

The sum in the parentheses of the second term on the right side of (A16) can be written as

$$\left(\frac{K}{2} - Y_{Lzn}\right)V_z^n. \tag{A17}$$

Substituting (A17) into (A16) gives (11).

The current $I_x^{n+1/2}$ is found similarly to yield (13) from the series node scattering relation (see Fig. 2(b)):

$$\begin{bmatrix} V_A \\ V_B \\ V_C \\ V_D \\ V_E \end{bmatrix}^r = [S]_S \begin{bmatrix} V_A \\ V_B \\ V_C \\ V_D \\ V_E \end{bmatrix}^i \tag{A18}$$

where

$$[S]_S = \frac{2}{M} \begin{bmatrix} -Z_{xzn,j+1} & Z_{xzn,j+1} & -Z_{xzn,j+1} & Z_{xzn,j+1} & Z_{xzn,j+1} \\ Z_{xzn} & -Z_{xzn} & Z_{xzn} & -Z_{xzn} & -Z_{xzn} \\ -Z_{xyn} & Z_{xyn} & -Z_{xyn} & Z_{xyn} & Z_{xyn} \\ Z_{xyn,k+1} & -Z_{xyn,k+1} & Z_{xyn,k+1} & -Z_{xyn,k+1} & -Z_{xyn,k+1} \\ Z_{Pxn} & -Z_{Pxn} & Z_{Pxn} & -Z_{Pxn} & -Z_{Pxn} \end{bmatrix} + [I] \tag{A19}$$

and

$$M \equiv Z_{xzn,j+1} + Z_{xzn} + Z_{xyn} + Z_{xyn,k+1} + Z_{Pxn}. \tag{A20}$$

ACKNOWLEDGMENT

The authors would like to thank M. Frankel, S. Gupta, G. Mourou, and J. Valdmanis of the Ultra-Fast Sciences Laboratory at The University of Michigan for providing electro-optic measurement data for the picosecond pulse generator. The reviewers are thanked for several suggestions which were helpful in improving the paper.

REFERENCES

[1] S. Akhtarzad and P. B. Johns, "Solution of Maxwell's equations in three space dimensions and time by the T.L.M. method of numerical analysis," *Proc. Inst. Elec. Eng.*, vol. 122, no. 12, pp. 1344–1348, Dec. 1975.

[2] A. Taflove and M. E. Brodwin, "Numerical solution of steady-state electromagnetic scattering problems using the time-dependent Maxwell's equations," *IEEE Trans. Microwave Theory Tech.*, vol. MTT-23, pp. 623–630, Aug. 1975.

[3] P. B. Johns, "On the relationship between TLM and finite-difference methods for Maxwell's equations," *IEEE Trans. Microwave Theory Tech.*, vol. MTT-35, pp. 60–61, Jan. 1987.

[4] J. Fang *et al.*, "Dispersion characteristics of microstrip lines in the vicinity of a coplanar ground," *Electron. Lett.*, vol. 23, no. 21, pp. 1142–1143, Oct. 8, 1987.

[5] T. A. Tumolillo and J. P. Wondra, "MEEC-3D: A computer code for self-consistent solution of the Maxwell–Lorentz equations in three dimensions," *IEEE Trans. Nuclear Sci.*, vol. NS-24, pp. 2449–2455, Dec. 1977.
[6] D. A. Al-Mukhtar and J. E. Sitch, "Transmission-line matrix method with irregularly graded space," *Proc. Inst. Elec. Eng.*, vol. 128, pt. H, no. 6, pp. 299–305, Dec. 1981.
[7] P. Saguet and S. Tedjini, "Méthode des lignes de transmission en trois dimensions: modification du processus de simulation," *Ann. Télécommun.*, vol. 40, no. 3–4, pp. 145–152, Mar.–Apr. 1985.
[8] W. K. Gwarek, "Comments on 'On the relationship between TLM and finite-difference methods for Maxwell's equations'," and reply by P. B. Johns, *IEEE Trans. Microwave Theory Tech.*, vol. MTT-35, pp. 872–873, Sept. 1987.
[9] P. B. Johns, "A new mathematical model to describe the physics of propagation," *Radio Electron. Eng.*, vol. 44, no. 12, pp. 657–666, Dec. 1974.
[10] G. E. Mariki and C. Yeh, "Dynamic three-dimensional TLM analysis of microstriplines on anisotropic substrate," *IEEE Trans. Microwave Theory Tech.*, vol. MTT-33, pp. 789–799, Sept. 1985.
[11] S. Koike, N. Yoshida, and I. Fukai, "Transient analysis of microstrip line on anisotropic substrate in three-dimensional space," *IEEE Trans. Microwave Theory Tech.*, vol. 36, pp. 34–43, Jan. 1988.
[12] N. Kukutsu, N. Yoshida, and I. Fukai, "Transient analysis of ferrite in three-dimensional space," *IEEE Trans. Microwave Theory Tech.*, vol. 36, pp. 114–125, Jan. 1988.
[13] T. Kashiwa, N. Yoshida, and I. Fukai, "Transient analysis of magnetized plasma in three-dimensional space," *IEEE Trans. Antennas Propagat.*, vol. 36, pp. 1096–1105, Aug. 1988.
[14] P. B. Johns and M. O'Brien, "Use of the transmission line modelling (T.L.M.) method to solve nonlinear lumped networks," *Radio Electron. Eng.*, vol. 50, nos. 1–2, pp. 59–70, Jan.–Feb. 1980.
[15] C. H. Hyun, M. S. Shur, and A. Peczalski, "Analysis of noise margin and speed of GaAs MESFET DCFL using UM-SPICE," *IEEE Trans. Electron Devices*, vol. ED-33, pp. 1421–1426, Oct. 1986.
[16] R. H. Voelker and R. J. Lomax, "Three-dimensional simulation of integrated circuits using a variable mesh TLM method," *Microwave and Opt. Technol. Lett.*, vol. 2, no. 4, pp. 125–127, Apr. 1989.
[17] R. H. Voelker and R. J. Lomax, "Three-dimensional electromagnetic field simulation of integrated circuits using the TLM method," in *Progress In Electromagnetics Research Symp. Proc.* (Boston), July 25–26, 1989, pp. 514–517.
[18] J. A. Valdmanis and G. Mourou, "Subpicosecond electrooptic sampling: Principles and applications," *IEEE J. Quantum Electron.* vol. QE-22, pp. 69–78, Jan. 1986.
[19] M. S. Shur, *GaAs Devices and Circuits*. New York: Plenum, 1987, pp. 472–475.
[20] M. S. Leong *et al.*, "Capacitance of shielded microstripline: Closed form quasi-TEM results suitable for computer-aided design," *Proc. Inst. Elec. Eng.*, vol. 134, pt. H., no. 4, pp. 393–396, Aug. 1987.

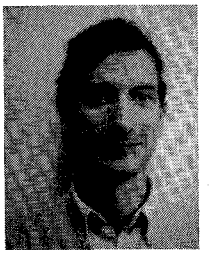

Robert H. Voelker (S'81–M'90) was born in Midland, MI, on May 30, 1960. In 1982 he received the B.S.E. degree (summa cum laude) and in 1983 the M.S.E. degree, both in electrical engineering, from the University of Michigan, Ann Arbor. He has just completed work for the Ph.D. degree in electrical engineering (awarded December 1989) at the University of Michigan. His research interests include computer-aided design of high-speed/high-frequency integrated circuits and their interconnections and supercomputing.

Dr. Voelker was an IBM Graduate Fellow for the 1983–84 academic year and a Shell Doctoral Fellow for the 1984–87 academic years. He is a member of Tau Beta Pi and Eta Kappa Nu.

Ronald J. Lomax (M'63–SM'69) was born in Stockport, England. He received the B.A. degree in mathematics in 1956, and the M.A. and Ph.D. degrees in applied mathematics in 1960, all from the University of Cambridge, England. From 1959 to 1961 he was a Bye-Fellow of Peterhouse, Cambridge.

Since 1961 he has been with the Solid State Electronics Laboratory (formerly Electron Physics Laboratory) at the University of Michigan, Ann Arbor. He is currently associated with the Center for High Frequency Microelectronics and is involved in research on high-speed GaAs digital circuits. He has served successively as Assistant Professor, Associate Professor, and currently Professor of Electrical Engineering and Computer Science. From 1977 to 1978 he was Visiting Professor at Stanford University. He has published in the areas of electron gun design, plasma simulation, microwave devices, finite difference and finite element simulation of solid-state devices, and CAD for VLSI. He has taught courses at the University of Michigan in physical electronics, integrated circuits, numerical methods, and VLSI design.

Dr. Lomax is a fellow of the Cambridge Philosophical Society and a member of the Society for Industrial and Applied Mathematics.